# Complete Single-Pass Conversion of Dilute Nitrate to Ammonia using Cu/Co(OH)<sub>2</sub> Tandem Electrocatalyst

Zhuanghe Ren, <sup>1</sup> Kaige Shi, <sup>1</sup> Zhen Meng, <sup>2</sup> Maia D. Willis, <sup>2</sup> and Xiaofeng Feng<sup>1,2,3,4</sup>\*

<sup>1</sup>Department of Physics, University of Central Florida, Orlando, Florida 32816, United States

<sup>2</sup>Department of Chemistry, University of Central Florida, Orlando, Florida 32816, United States

<sup>3</sup>Renewable Energy and Chemical Transformations (REACT) Cluster, University of Central Florida, Orlando, Florida 32816, United States

<sup>4</sup>Department of Materials Science and Engineering, University of Central Florida, Orlando, Florida 32816, United States

\*Email: Xiaofeng.Feng@ucf.edu (X.F.)

#### **ABSTRACT:**

Electrochemical nitrate reduction reaction (NO<sub>3</sub>RR) provides a promising route for the denitrification of wastewater and sustainable NH<sub>3</sub> production, but requires active and selective electrocatalysts. Here, we demonstrate a rigorous design of tandem electrocatalyst for efficient conversion of NO<sub>3</sub><sup>-</sup> to NH<sub>3</sub>. Based on the screening of tandem components, a catalyst coupling Cu and Co(OH)<sub>2</sub> with an optimal ratio and tandem architecture was developed to promote and balance the activities of sequential NO<sub>3</sub>RR steps on different active sites. Compared to counterpart catalysts including Cu, Co(OH)<sub>2</sub>, and Cu-Co alloy, the Cu/Co(OH)<sub>2</sub> catalyst with separated phases showed much higher activity and selectivity for NO<sub>3</sub>RR to NH<sub>3</sub>, suggesting a tandem mechanism that involves NO<sub>3</sub><sup>-</sup> reduction to NO<sub>2</sub><sup>-</sup> on Cu and solution transfer and further reduction of NO<sub>2</sub><sup>-</sup> to NH<sub>3</sub> on Co-based sites. When operated in a flow cell, the Cu/Co(OH)<sub>2</sub> catalyst further achieved 100% single-pass conversion of dilute NO<sub>3</sub><sup>-</sup> solution to NH<sub>3</sub> at low overpotentials.

The development of the Haber–Bosch process opened the door to large-scale production of ammonia (NH<sub>3</sub>) and thus boosted the production of nitrogen fertilizers, which has significantly increased the global agricultural yield. However, the nitrogen use efficiency of the fertilizers is typically lower than 40%, <sup>1</sup> so that the nitrogen readily leaches out of soil and enters groundwater, lakes, and rivers. The excessive use of agricultural fertilizers as well as the discharge of industrial wastewater has substantially increased the concentration of nitrate (NO<sub>3</sub><sup>-</sup>) in the world water bodies, <sup>2</sup> causing serious environmental problems such as eutrophication and disturbance of ecosystems. <sup>3</sup> Aiming at the denitrification of wastewater, the electrochemical reduction of nitrate has recently emerged as a promising strategy, <sup>4-6</sup> as it can be powered by renewable electricity with NH<sub>3</sub> as a major product, which may thus provide a sustainable route for NH<sub>3</sub> production as an alternative to the energy- and carbon-intensive Haber–Bosch process. <sup>7-9</sup>

The electrochemical nitrate reduction reaction (NO<sub>3</sub>RR) to NH<sub>3</sub> involves the transfer of eight electrons and consecutive hydrogenation and deoxygenation steps:  $NO_3^- + 6H_2O + 8e^- \rightarrow NH_3 + 9OH^-$ . As a result, a relatively high overpotential is needed to overcome the kinetic barrier of the reaction, particularly for the  $NO_3^-$ -to- $NO_2^-$  step that is often considered to be the rate-determining step.<sup>4</sup> In addition to NH<sub>3</sub>, the NO<sub>3</sub>RR generates other undesired side products including  $NO_2^-$ ,  $N_2$ ,  $N_2O$ , and  $NH_2OH$ .<sup>4,5</sup> Among them,  $NO_2^-$  is a main side product that lowers the Faradaic efficiency for NH<sub>3</sub> production, while the intermediately produced  $NO_2^-$  can be further reduced to NH<sub>3</sub> on the electrode, <sup>10</sup> suggesting a unique dual role of  $NO_2^-$  in the  $NO_3RR$  catalysis. Furthermore, hydrogen evolution reaction (HER) may occur simultaneously and compete with the  $NO_3RR$  under more negative potentials. Therefore, the development of efficient electrocatalysts for the  $NO_3RR$  to  $NH_3$  encounters challenges in both activity and selectivity.

To date, a variety of electrocatalysts have been investigated for the NO<sub>3</sub>RR, including Cu, Co, Pd, Ru, Ti, and carbon-based materials,<sup>11–23</sup> and different strategies have been utilized to improve their electrocatalytic performance.<sup>24–35</sup> In particular, a concept of tandem catalysis was proposed, where two distinct catalytic sites are coupled to accelerate the NO<sub>3</sub><sup>-</sup>-to-NO<sub>2</sub><sup>-</sup> and NO<sub>2</sub><sup>-</sup>-to-NH<sub>3</sub> steps, respectively, thus to improve the overall efficiency for the NO<sub>3</sub>RR to NH<sub>3</sub>. Recently, this concept has been implemented in the development of some catalyst systems such as Cu-Co, Cu-Ru, and Ru-Co based materials,<sup>36–41</sup> which achieved efficient NO<sub>3</sub>RR with a high activity and NH<sub>3</sub> Faradaic efficiency. However, those tandem catalysts were mainly developed based on empirical considerations, while a more rational and rigorous design and a deeper mechanism understanding of the NO<sub>3</sub>RR process on tandem catalysts are still needed. Moreover, the NO<sub>3</sub>RR performance was typically evaluated in an H-cell setup, which has a gap with the need of continuous electrolysis for practical applications, so the operation in a flow cell particularly with a single-pass mode is highly desired.<sup>42,43</sup> While high yields of NH<sub>3</sub> may be reached using electrolytes with a high NO<sub>3</sub><sup>-</sup> concentration (0.1–1 M),<sup>44–48</sup> typical nitrate sources such as industrial runoff and polluted ground

water, have a low NO<sub>3</sub><sup>-</sup> concentration ranging from few to few tens of mM,<sup>49–51</sup> so an efficient electrolysis of diluted nitrate to ammonia is of vital importance for practical applications.<sup>52</sup>

In this work, we present a rigorous design of tandem electrocatalyst for efficient conversion of dilute nitrate to ammonia. We first screen and identify the catalyst components for the initial reduction of NO<sub>3</sub><sup>-</sup> and the further reduction of NO<sub>2</sub><sup>-</sup> intermediate. Based on the screening results, a Cu/Co(OH)<sub>2</sub> tandem catalyst is prepared by deposition of Co(OH)<sub>2</sub> nanosheets on a Cu substrate with an optimal ratio and structure, thus to promote and balance the activities of the NO<sub>3</sub><sup>-</sup>-to-NO<sub>2</sub><sup>-</sup> and NO<sub>2</sub><sup>-</sup>-to-NH<sub>3</sub> steps. Compared to counterpart catalysts including Cu, Co(OH)<sub>2</sub>, and Cu-Co alloy, the Cu/Co(OH)<sub>2</sub> catalyst with separated phases shows a much higher activity and selectivity for the NO<sub>3</sub>RR to NH<sub>3</sub>, suggesting a tandem catalytic mechanism that involves NO<sub>3</sub><sup>-</sup> reduction to NO<sub>2</sub><sup>-</sup> on Cu, indirect transfer of NO<sub>2</sub><sup>-</sup> via the electrolyte, and NO<sub>2</sub><sup>-</sup> reduction to NH<sub>3</sub> on Co-based sites. Using a flow cell, the Cu/Co(OH)<sub>2</sub> catalyst further achieves 100% single-pass conversion of NO<sub>3</sub><sup>-</sup> to NH<sub>3</sub> at -0.1 V vs the reversible hydrogen electrode (RHE, all potentials are reported with respect to this reference in this work) for continuous NO<sub>3</sub>RR electrolysis.

Selection of tandem catalyst components. As the NO<sub>3</sub>RR involves multiple electron transfer and hydrogenation steps, a single-component catalyst may only exhibit appreciable activity for certain step of the reaction, typically NO<sub>3</sub><sup>-</sup>-to-NO<sub>2</sub><sup>-</sup> or NO<sub>2</sub><sup>-</sup>-to-NH<sub>3</sub> (Figure 1a), due to the limitation of a linear scaling relationship between the binding energies of different intermediates on a catalyst surface. 12,28,53 In contrast, a tandem catalyst can couple two active sites to promote the two steps simultaneously (Figure 1b), thus to achieve efficient and selective NO<sub>3</sub>RR to NH<sub>3</sub>. We first identify the components that are highly active for each step by screening various transition metals. Here, polycrystalline metal foils were used as a model catalyst to minimize the influence of electrode area and morphology and thus to compare their intrinsic activities.<sup>23</sup> The metal foil electrodes were tested for the NO<sub>3</sub>RR and NO<sub>2</sub><sup>-</sup> reduction reaction (NO<sub>2</sub>RR) in 1 M KOH electrolytes containing 5 mM KNO<sub>3</sub> and 5 mM KNO<sub>2</sub>, respectively. Linear sweep voltammetry (LSV) was first performed to evaluate the metal electrodes in a two-compartment electrochemical cell (H-cell), as shown in Figure S1. The current densities measured on the electrodes in the presence of NO<sub>3</sub><sup>-</sup> (Figure 1c) are much higher than that in 1 M KOH electrolyte without NO<sub>3</sub><sup>-</sup> (Figure S2), confirming their activities for the NO<sub>3</sub>RR. As exhibited in Figure 1c, the LSV curves recorded on the metal electrodes indicate an increase of the NO<sub>3</sub>RR activity in this order: Ni < Fe < Pd < Co < Cu. Particularly, the NO<sub>3</sub>RR on Cu showed an onset potential of 0.2 V vs RHE and reached a plateau at around -0.1 V in the LSV curve, while the current densities on Pd, Fe, and Ni were negligible at -0.1 V. In comparison, the NO<sub>2</sub>RR activity on the metal electrodes showed a distinct trend and increased in the order: Pd < Fe < Cu < Ni < Co, as indicated by the LSV curves in Figure 1d. The NO<sub>2</sub>RR on Cu showed a reduction peak at -0.1 V and then reached a plateau at -0.25 V, which should be attributed to the coexistence of Cu(100) and Cu(111) facets<sup>23</sup> that have

different NO<sub>2</sub>RR activities.<sup>11</sup> Among these metals, Cu showed the highest activity for the initial reduction of NO<sub>3</sub><sup>-</sup> but a lower activity for the subsequent reduction of NO<sub>2</sub><sup>-</sup>. On the other hand, while Co is less active than Cu in initiating the NO<sub>3</sub>RR, it showed the highest activity for the NO<sub>2</sub>RR, standing out as the most active metal for the NO<sub>2</sub><sup>-</sup>-to-NH<sub>3</sub> step among these candidates. Therefore, Cu and Co are complementary to each other in the electrocatalytic process, and a tandem catalyst coupling Cu and Co may achieve both high activity and selectivity for efficient NO<sub>3</sub>RR to NH<sub>3</sub>.

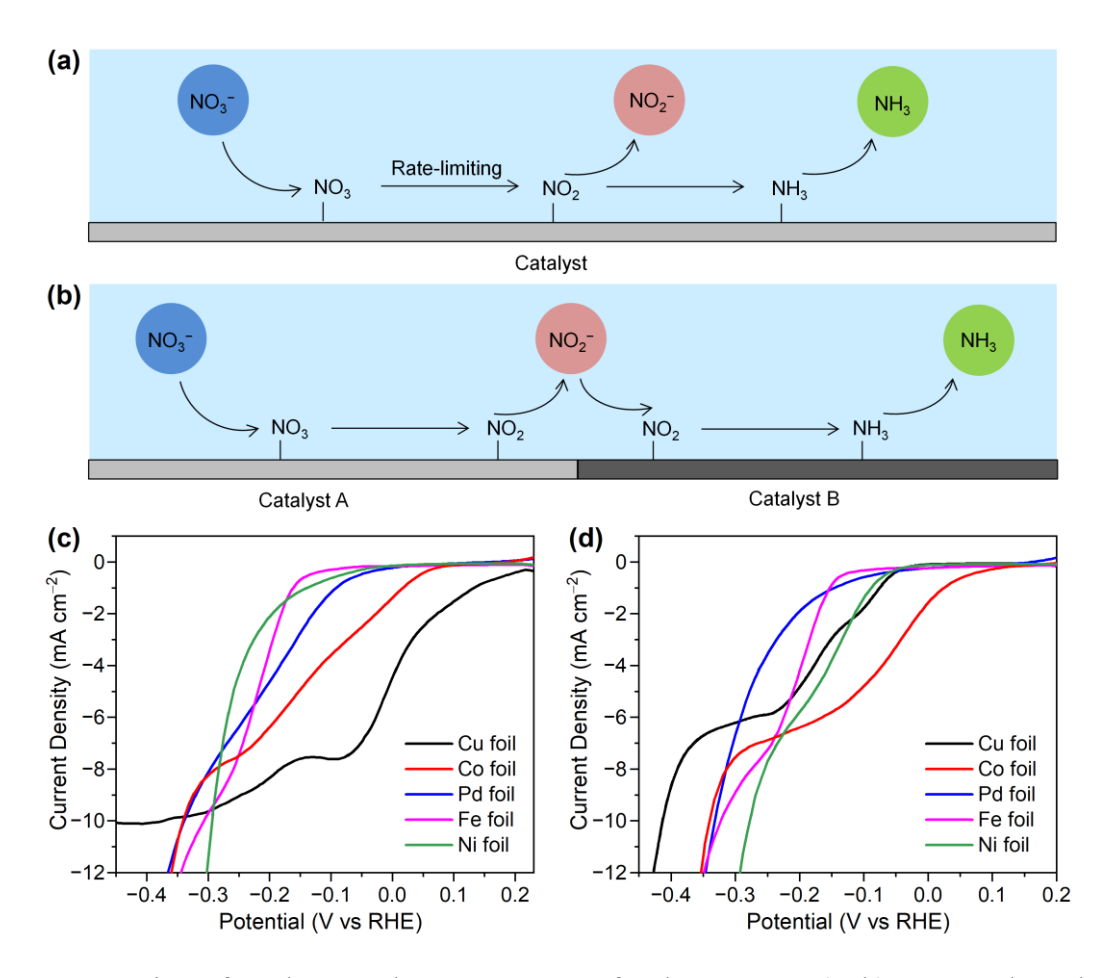


**Figure 1.** Screening of tandem catalyst components for the  $NO_3RR$ . (a–b) Proposed mechanisms for the  $NO_3RR$  on single-component (a) and tandem (b) electrocatalysts. (c–d) LSV curves recorded on different metal foil electrodes in 1 M KOH + 5 mM KNO<sub>3</sub> (c) and 1 M KOH + 5 mM KNO<sub>2</sub> (d) electrolytes, respectively. Scan rate: 5 mV s<sup>-1</sup>.

**Preparation and characterization of Cu/Co(OH)**<sub>2</sub> **tandem catalyst.** To develop the proposed tandem catalyst, we need to find the suitable Co-based material as a tandem component, as recent studies suggest that Co(OH)<sub>2</sub> may be reduced to Co during NO<sub>3</sub>RR, forming a dynamic Co valence cycle. <sup>10,40</sup> To examine the possible chemical state evolution of Co, we tested a Co foil electrode

for NO<sub>3</sub>RR in 1 M KOH + 5 mM KNO<sub>3</sub> electrolyte at -0.15 V vs RHE, and characterized it before and after the NO<sub>3</sub>RR test. As shown by the scanning electron microscopy (SEM) images and Xray photoelectron spectra (XPS) in Figure S3, the Co foil surface mostly changed to Co(OH)<sub>2</sub> after the NO<sub>3</sub>RR test, as indicated by the nanosheet morphology and the chemical state of Co. To further identify the active Co state during NO<sub>3</sub>RR, we prepared Co nanoparticles (Figure S4) and Co(OH)<sub>2</sub> nanosheets on carbon support (Figure S5) and performed operando X-ray absorption spectroscopy (XAS) characterization of the electrocatalysts during NO<sub>3</sub>RR (Figure S6). As shown in Figure S7, both X-ray absorption near edge structure (XANES) spectra and Fourier-transformed extended Xray absorption fine structure (FT-EXAFS) spectra of Co K-edge indicate that Co(OH)<sub>2</sub> has a better stability than Co nanoparticles under the electrolysis conditions. Therefore, we deposited Co(OH)<sub>2</sub> nanosheets on a Cu foam substrate using an electrochemical deposition method to prepare model tandem catalysts (see Experimental Methods for details).<sup>54</sup> A series of Cu/Co(OH)<sub>2</sub> samples were prepared with the Co(OH)<sub>2</sub> deposition time varying from 0 to 60 min, for the comparison and optimization of the Cu:Co ratio. A representative sample with 50-min deposition time was selected for the characterization of morphology, structure, and chemical state. As presented in Figure 2a and Figure S8a, the SEM images showed a bare surface of the Cu foam, which was evenly covered with numerous nanosheets after the deposition of Co(OH)<sub>2</sub> (Figure 2b and Figure S9). The uniform distribution of Co species on the Cu surface was also confirmed by the energy-dispersive X-ray spectroscopy (EDS) mapping in Figure S10. Grazing-incidence X-ray diffraction (XRD) pattern was further obtained for the Cu/Co(OH)2 sample, as shown in Figure 2c, which exhibited a new and broad peak centered at 10.5° as compared to that of the Cu foam (Figure S8b). This diffraction peak was attributed to α-Co(OH)<sub>2</sub> (001) planes, <sup>54</sup> so the nanosheets on the Cu foam were identified to be  $\alpha$ -Co(OH)<sub>2</sub>.

The chemical state of the Cu/Co(OH)<sub>2</sub> sample was further examined by XPS and Raman spectroscopy (Figure 2d–f). Both Co 2p XPS spectra (Figure 2e) and characteristic peaks in the Raman spectra (Figure 2f) confirmed the presence of Co(OH)<sub>2</sub> on the Cu foam, <sup>55,56</sup> while the Cu foam surface encountered some minor oxidation during the preparation, as indicated by the characteristic peaks of Cu<sup>2+</sup> in the Cu 2p XPS spectra (Figure 2d and Figure S8c–d).<sup>57</sup> As Cu oxides can be reduced during the NO<sub>3</sub>RR and may impact the determination of Faradaic efficiency, an electrochemical pre-reduction was performed to remove surface oxides by cyclic voltammetry (CV) scans from 0 to –0.45 V vs RHE in a 1 M KOH electrolyte. After the pre-reduction treatment, the Cu 2p XPS spectra revealed a decrease of the amount of Cu oxides (Figure 2d), along with a partial conversion of Co(OH)<sub>2</sub> to CoO (Figure 2e,f).<sup>10,58</sup> As the chemical state of electrocatalysts may evolve during electrolysis, the electrode was also characterized after being tested for the NO<sub>3</sub>RR (Figure 2d–f), where only metallic Cu and Co(OH)<sub>2</sub> remained on the electrode surface. Therefore, the sample is hereafter referred to as Cu/Co(OH)<sub>2</sub>, which should reflect the composition and chemical state of the electrocatalyst during NO<sub>3</sub>RR.

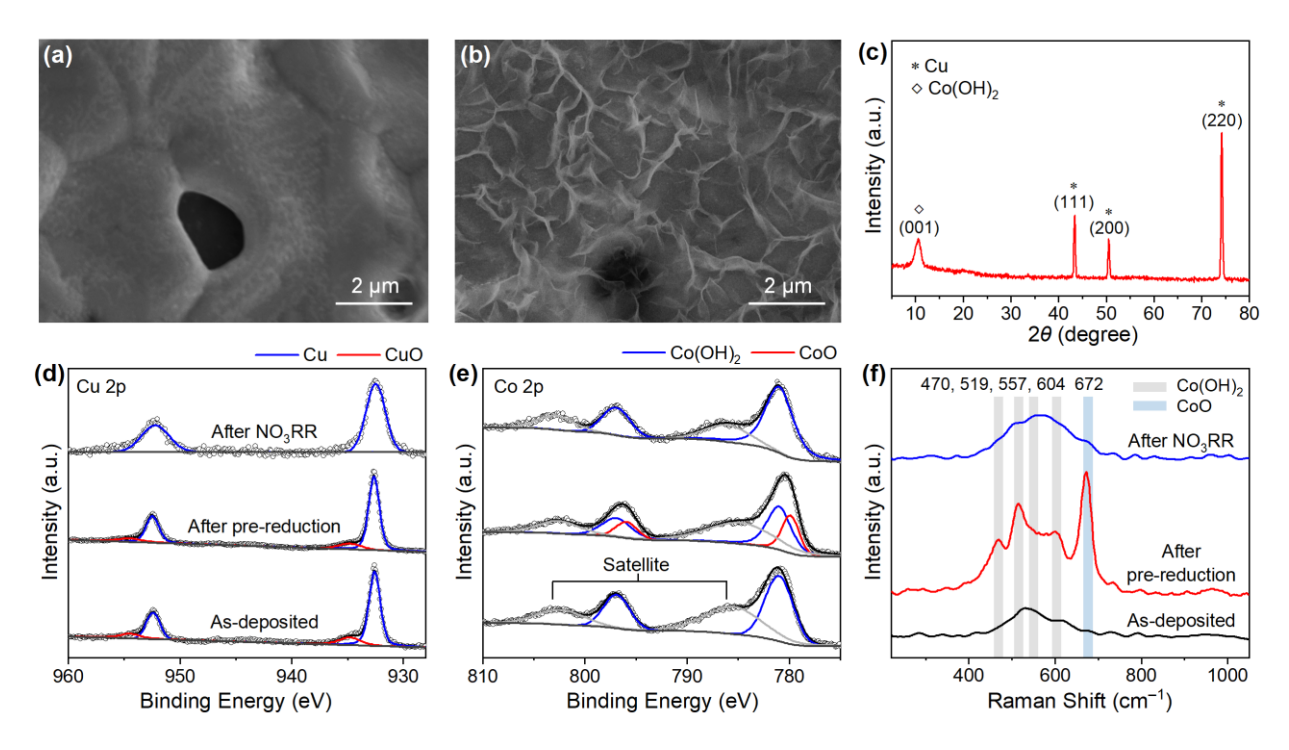


**Figure 2.** Characterizations of the Cu/Co(OH)<sub>2</sub> catalyst. (a) SEM image of the Cu foam. (b) SEM image and (c) grazing-incidence XRD pattern of the Cu/Co(OH)<sub>2</sub> sample prepared with 50-min deposition time. (d–f) XPS spectra of the Cu 2p (d) and Co 2p (e) regions and Raman spectra (f) of the Cu/Co(OH)<sub>2</sub> sample under different conditions (as-deposited, after pre-reduction, and after NO<sub>3</sub>RR). The deconvoluted peaks of the XPS spectra were fitted using the Gaussian fitting method.

Activity balance between NO<sub>3</sub><sup>-</sup>-to-NO<sub>2</sub><sup>-</sup> and NO<sub>2</sub><sup>-</sup>-to-NH<sub>3</sub>. As the Cu and Co(OH)<sub>2</sub> components are designed to promote the NO<sub>3</sub><sup>-</sup>-to-NO<sub>2</sub><sup>-</sup> and NO<sub>2</sub><sup>-</sup>-to-NH<sub>3</sub> steps, respectively, a balance or match between the rates of the two steps is needed to reach the best efficacy of tandem catalysis. Otherwise, an excessive amount of Cu will generate too much NO<sub>2</sub><sup>-</sup> and thus lower the Faradaic efficiency for NH<sub>3</sub> production, while a too high ratio of Co(OH)<sub>2</sub> will lead to slow NO<sub>3</sub><sup>-</sup> reduction and thus a low activity. Such an activity balance can be achieved by optimizing the Cu:Co ratio on the electrode surface. To find the optimal Cu:Co ratio, we varied the amount of Co(OH)2 on Cu foam by changing the deposition time at a fixed deposition rate of -0.1 mA cm<sup>-2</sup>. As the deposition time increased from 10 to 60 min, SEM images showed that the Cu foam surface evolved from a nearly bare state to that with a dense coverage of Co(OH)<sub>2</sub> nanosheets, as exhibited in Figure 3a. EDS spectra were acquired on the Cu/Co(OH)<sub>2</sub> samples prepared with different deposition times, as exhibited in Figure S11. The EDS analysis indicated that the Co content increased monotonically with the deposition time, reaching ~44 at% at 50 min and then surpassing the Cu content at 60 min. As EDS is not a very surface sensitive technique, we further performed XPS characterization of the Cu/Co(OH)<sub>2</sub> samples to check the surface composition. As shown in Figure S12, high-resolution XPS spectra of the Cu 2p and Co 2p regions of the samples give a relatively

lower surface ratio of Cu, but it is still confirmed that the relative ratio of Co to Cu increased along with the increase of deposition time. The Cu/Co(OH)<sub>2</sub> samples were evaluated for NO<sub>3</sub>RR by bulk electrolysis in an H-cell with a 1 M KOH + 5 mM KNO<sub>3</sub> electrolyte. Possible gas-phase products (such as H<sub>2</sub> and N<sub>2</sub>) were examined by gas chromatography. Two products, NH<sub>3</sub> and NO<sub>2</sub><sup>-</sup>, were identified in the catholyte and quantified by the indophenol blue method<sup>59</sup> and Griess method,<sup>60</sup> respectively, based on the calibration curves in Figures S13 and S14. The quantification of NH<sub>3</sub> production was also verified by <sup>1</sup>H nuclear magnetic resonance (NMR) spectroscopy, based on the calibration curves in Figure S15. Moreover, the N source of the detected ammonia was confirmed to be the nitrate in the electrolyte using <sup>15</sup>N isotope labeling experiment.

We compared the NO<sub>3</sub>RR activity and selectivity on those electrodes at -0.05 V vs RHE, as shown in Figure 3c. Along with the increase of Co(OH)<sub>2</sub> deposition time, the total current density first increased from 2.1 mA cm<sup>-2</sup> on the Cu foam to 18.2 mA cm<sup>-2</sup> on the Cu/Co(OH)<sub>2</sub> electrode with 50-min deposition time, but then declined to 12.2 mA cm<sup>-2</sup> on the electrode with even more deposition (60 min). Meanwhile, the NH<sub>3</sub> Faradaic efficiency increased rapidly from 35.5% on the Cu foam to 96.2% on the Cu/Co(OH)<sub>2</sub> electrode with 50-min deposition time, and then remained unchanged on the 60-min sample. Clearly, the deposited Co(OH)<sub>2</sub> greatly improved both activity and selectivity for the NO<sub>3</sub>RR to NH<sub>3</sub>, which should benefit from the high activity for the initial reduction of NO<sub>3</sub><sup>-</sup> on Cu and the enhanced reduction of NO<sub>2</sub><sup>-</sup> to NH<sub>3</sub> on Co-based sites. <sup>10,40</sup> As predicted above, a too high ratio of Co in the 60-min sample led to a decline of the activity, due to the insufficient amount of Cu surface for the initial reduction of NO<sub>3</sub><sup>-</sup>. Meanwhile, the 60-min sample still showed a 96% Faradaic efficiency for NH<sub>3</sub> production, indicating that Co(OH)<sub>2</sub> is very selective for NO<sub>3</sub>RR to NH<sub>3</sub>. To elucidate this, we deposited Co(OH)<sub>2</sub> nanosheets on carbon paper as an inert substrate (Figure S5), thus to evaluate its performance in the absence of Cu. The carbonsupported Co(OH)<sub>2</sub> sample exhibited a much lower NO<sub>3</sub>RR activity than that of the Cu/Co(OH)<sub>2</sub> sample, as shown in Figure S16, confirming the requirement of both Cu and Co(OH)<sub>2</sub> to achieve highly active and selective NO<sub>3</sub>RR. Interestingly, Co(OH)<sub>2</sub> showed a much higher activity for the NO<sub>2</sub>RR than NO<sub>3</sub>RR, so Co(OH)<sub>2</sub> is highly active in reducing NO<sub>2</sub><sup>-</sup> to NH<sub>3</sub> and can complement Cu to achieve the tandem catalysis. Thus, the Cu/Co(OH)<sub>2</sub> electrode with a 50-min deposition time exhibited the best performance for NO<sub>3</sub>RR, suggesting an optimal Cu:Co ratio in the sample for efficient tandem catalysis.

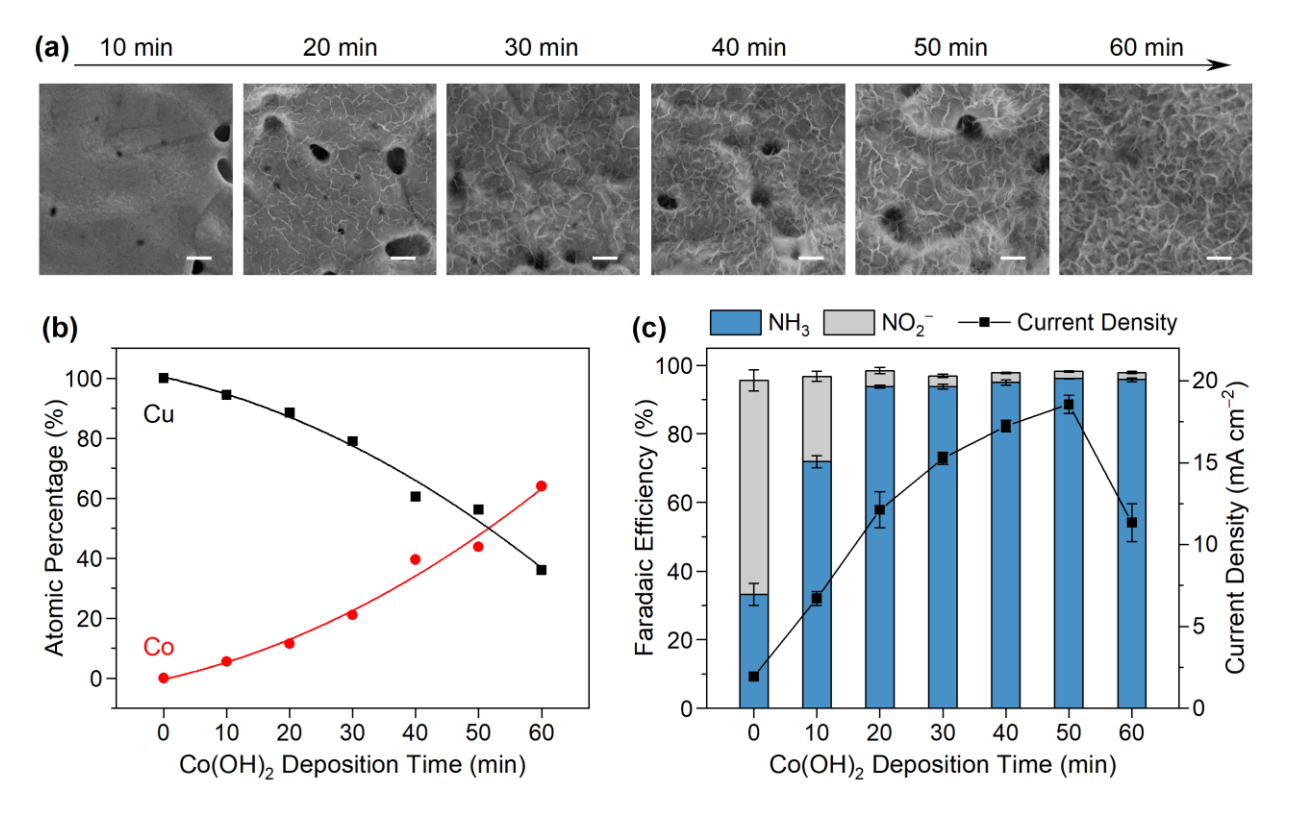


**Figure 3.** Effect of the Cu:Co ratio in the Cu/Co(OH)<sub>2</sub> catalyst for the NO<sub>3</sub>RR. (a–b) SEM images (a) and atomic percentages (b) of Cu/Co(OH)<sub>2</sub> samples prepared with various Co(OH)<sub>2</sub> deposition times. All scale bars in (a) are 2  $\mu$ m. (c) Current density and Faradaic efficiency for NO<sub>3</sub>RR on the Cu/Co(OH)<sub>2</sub> electrodes at –0.05 V vs RHE in H-cell with 1 M KOH + 5 mM KNO<sub>3</sub> electrolyte. The error bars represent the standard deviation of three independent measurements.

Tandem catalyst architecture. The above Cu/Co(OH)<sub>2</sub> catalyst demonstrated a tandem effect on the NO<sub>3</sub>RR, which also raised the following question: which tandem architecture, separated phases or atomically mixed (alloy), is more efficient for the NO<sub>3</sub>RR? Comparing the efficacy of the two tandem architectures on the NO<sub>3</sub>RR can help elucidate the tandem catalysis mechanism: does the transfer of \*NO<sub>2</sub> intermediates from Cu to Co sites occur via direct surface diffusion or an indirect route (desorb from Cu sites, enter the electrolyte as NO<sub>2</sub><sup>-</sup>, and re-adsorb on Co sites), as illustrated in Figure 4a? If it is the former case (direct transfer), atomically mixed Cu-Co alloy should show a higher activity and NH<sub>3</sub> selectivity than the separated phases of Cu/Co(OH)<sub>2</sub> due to the adjacent Cu and Co sites. For a comparative study, Cu-Co alloy nanoparticles were prepared using a wet impregnation method followed by thermal reduction (see Experimental Methods for details).<sup>61</sup> The formation of Cu-Co alloy, rather than segregated phases, was confirmed by transmission electron microscopy (TEM) imaging and XRD pattern, as shown in Figure S17. The ratio of Cu to Co on the surface of Cu-Co alloy was also probed by XPS (Figure S18), which is similar to that of the Cu/Co(OH)<sub>2</sub> sample. Furthermore, *operando* XAS characterization was performed to examine the

active state of Co in the two samples during NO<sub>3</sub>RR. As shown in Figure S19, the chemical state of Co in the Cu/Co(OH)<sub>2</sub> sample changed significantly from open circuit potential (OCP) to -0.1 V vs RHE, at which the Co–Co characteristic peak became dominant in the FT-EXAFS, indicating a reduction of Co(OH)<sub>2</sub> to Co<sup>0</sup>. This is distinct from the carbon-supported Co(OH)<sub>2</sub> sample, where the Co–O peak and Co state remained largely unchanged from OCP to -0.1 V vs RHE (Figure S7). Thus, the presence of Cu can promote the electroreduction of Co(OH)<sub>2</sub> to Co<sup>0</sup>, which is consistent with the observation with RuCo catalyst for NO<sub>3</sub>RR. <sup>40</sup> More importantly, the Cu-Co alloy reached a similar Co state at -0.1 V vs RHE, as indicated by the FT-EXAFS in Figure S19d. Therefore, the Cu/Co(OH)<sub>2</sub> and Cu-Co alloy samples can be compared to study the effect of tandem architecture or atomic arrangement. In addition, the Cu foam and carbon-supported Co(OH)<sub>2</sub> sample were also included in the comparison as reference samples.

The Cu-Co alloy, Cu foam, and Co(OH)<sub>2</sub> samples were evaluated for the NO<sub>3</sub>RR at selected potentials, and then compared to the Cu/Co(OH)<sub>2</sub> sample prepared with 50-min deposition time. The NO<sub>3</sub>RR electrolysis was similarly performed in an H-cell with a 1 M KOH + 5 mM KNO<sub>3</sub> electrolyte. As shown in Figure 4b, the current density on the Cu-Co alloy increased from 3.9 to  $9.0 \text{ mA cm}^{-2}$  as the potential shifted from 0 to -0.15 V vs RHE, which was higher than that on the Cu foam and Co(OH)<sub>2</sub> sample, but much lower than that on the Cu/Co(OH)<sub>2</sub> electrode. Meanwhile, the current density on Cu/Co(OH)<sub>2</sub> increased rapidly from 5.3 mA cm<sup>-2</sup> at 0 V to 18.2 mA cm<sup>-2</sup> at -0.05 V, and then reached a plateau ( $\sim$ 19.7 mA cm<sup>-2</sup>) at more negative potentials due to the mass transport limitation of NO<sub>3</sub><sup>-</sup> (5 mM), showing a much higher activity than the Cu-Co alloy. The NH<sub>3</sub> Faradaic efficiency was similar between the Cu-Co alloy and Cu/Co(OH)<sub>2</sub> at potentials from 0 to -0.1 V (Figure 4c), which however declined to 78% on the Cu-Co alloy at -0.15 V due to the emergence of the HER activity. In contrast, the Cu/Co(OH)<sub>2</sub> electrode achieved an ultrahigh NH<sub>3</sub> Faradic efficiency of 99% at -0.15 V. The HER activity of the Cu-Co alloy is higher than Co, as confirmed by the LSV curves recorded on the CuCo alloy and Co nanoparticles in Ar-purged 1 M KOH electrolyte (Figure S20), which is attributed to the metal alloying that changed the electronic structure. 62 Therefore, the Cu-Co alloy exhibited a low NO<sub>3</sub>RR activity but a high NH<sub>3</sub> selectivity, as well as a high HER activity. 10,40 Although the Cu-Co alloy showed a better performance than Cu and Co(OH)<sub>2</sub>, it could not combine the electrocatalytic strengths of Cu and Co(OH)<sub>2</sub> to achieve efficient tandem catalysis. Thus, the separated tandem architecture was found to be more favorable for the NO<sub>3</sub>RR to NH<sub>3</sub>, where Cu and Co(OH)<sub>2</sub> can largely maintain their own catalytic properties. Here, the Cu/Co(OH)<sub>2</sub> and Cu-Co alloy samples have similar surface Cu-to-Co ratios (XPS data) and similar Co state during NO<sub>3</sub>RR (XAS data in Figure S19), so we can compare their intrinsic activities to identify the mechanism: whether the transfer of \*NO2 intermediates from the Cu site to the Co site is achieved by direct surface diffusion or by an indirect route. As the Cu-Co alloy showed a lower NO<sub>3</sub>RR activity (Figure 4b), it is deduced that the adjacent Cu and Co sites in the alloy did not promote the transfer of \*NO<sub>2</sub> intermediates via surface diffusion. We can thus propose

that the transfer of \*NO<sub>2</sub> intermediates from Cu to Co sites in the tandem catalytic process mainly occurs via an indirect route (enter the electrolyte as NO<sub>2</sub><sup>-</sup> and then re-adsorb on the Co sites), as will be further discussed below.

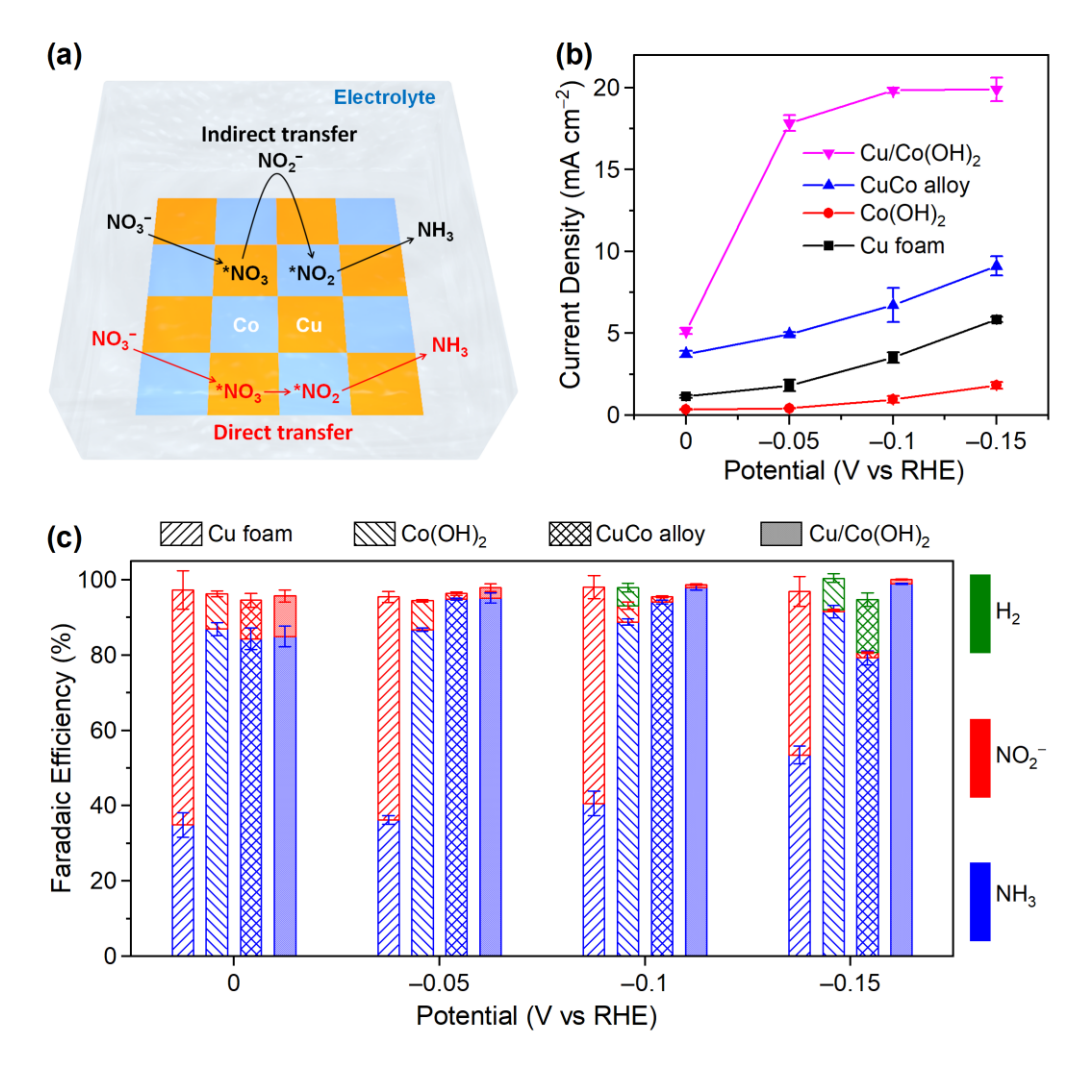


**Figure 4.** Effect of tandem catalyst architecture. (a) Schematic illustration of the possible tandem mechanisms for NO<sub>3</sub>RR on Cu-Co-based catalyst. (b) Current density and (c) Faradaic efficiency for the NO<sub>3</sub>RR on the Cu foam, Co(OH)<sub>2</sub> sample, Cu-Co alloy, and Cu/Co(OH)<sub>2</sub> tandem catalyst at selected potentials in H-cell with 1 M KOH + 5 mM KNO<sub>3</sub> electrolyte. The error bars represent the standard deviation of three independent measurements.

**Single-pass conversion of NO<sub>3</sub>**<sup>-</sup> using tandem catalyst. The applications of the NO<sub>3</sub>RR catalysts will eventually require a single-pass conversion of NO<sub>3</sub><sup>-</sup> to NH<sub>3</sub>. To test the single-pass conversion rate of NO<sub>3</sub>RR, a homebuilt flow cell was developed for continuous NO<sub>3</sub>RR electrolysis, as shown in Figure S21. The above designed Cu/Co(OH)<sub>2</sub> catalyst was first evaluated for continuous NO<sub>3</sub>RR electrolysis in the flow cell. As shown in Figure S22, although the Cu/Co(OH)<sub>2</sub> catalyst exhibited

a high activity and selectivity for NO<sub>3</sub>RR to NH<sub>3</sub>, the single-pass conversion rate was low, which only reached 17% at an electrolyte flow rate of 30 mL h<sup>-1</sup> and further dropped at higher flow rates. To enhance the single-pass conversion rate, we improved the catalyst design by first growing Cu nanowires on a Cu foam and then depositing Co(OH)2 nanosheets on the Cu nanowires, thus to increase the electrochemical surface area (ECSA) of the electrode. The CuNW/Co(OH)2 electrode was prepared by the growth of CuO nanowires on a Cu foam (SEM image in Figure 5a), 63 and then electrochemical deposition of Co(OH)<sub>2</sub> nanosheets (SEM image in Figure 5b),<sup>54</sup> followed by the electroreduction of CuO to Cu nanowires (see Experimental Methods for details).<sup>64</sup> The TEM image and EDS mapping in Figure 5c confirmed the coupling between Cu nanowires and Co(OH)<sub>2</sub> nanosheets. Due to the increase of Cu surface area, here the Co(OH)2 deposition was performed at a higher current density of -0.2 mA cm<sup>-2</sup> with the deposition time to be optimized again. As a result, the CuNW/Co(OH)<sub>2</sub> electrode prepared with 45-min deposition time showed an optimal performance for NO<sub>3</sub>RR and was thus selected for further study below. The ECSA of an electrode is proportional to its double-layer capacitance, which can be measured by a CV method. As shown in Figure S23, the double-layer capacitance of the CuNW/Co(OH)2 electrode is around 6 times that of the Cu/Co(OH)<sub>2</sub> electrode, confirming a significant increase of the ECSA.

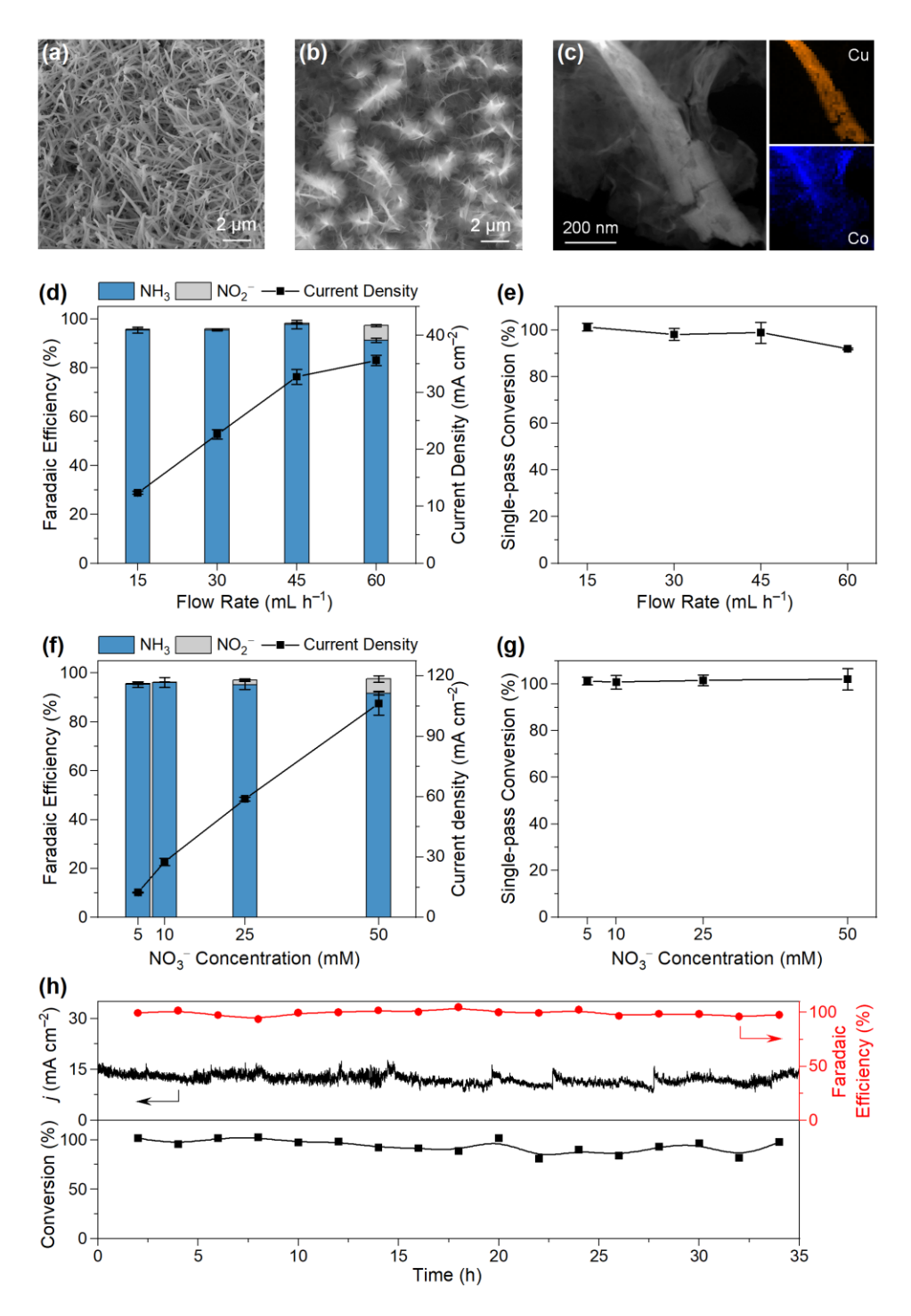


**Figure 5.** Single-pass conversion of NO<sub>3</sub><sup>−</sup> to NH<sub>3</sub> on the CuNW/Co(OH)<sub>2</sub> catalyst in flow cell. (a) SEM image of the Cu nanowires grown on Cu foam. (b) SEM image and (c) TEM image and corresponding EDS mapping of the CuNW/Co(OH)<sub>2</sub> sample prepared with 45-min deposition time. (d) Current density and Faradaic efficiency, and (e) single-pass conversion rate for the NO<sub>3</sub>RR on CuNW/Co(OH)<sub>2</sub> at −0.1 V vs RHE in a flow cell with 1 M KOH + 5 mM KNO<sub>3</sub> electrolyte at various flow rates. (f) Current density and Faradaic efficiency, and (g) single-pass conversion rate

for the NO<sub>3</sub>RR on CuNW/Co(OH)<sub>2</sub> at -0.1 V vs RHE in a flow cell with 1 M KOH electrolytes containing different concentrations of NO<sub>3</sub><sup>-</sup> at a flow rate of 15 mL h<sup>-1</sup>. (h) Stability test of the CuNW/Co(OH)<sub>2</sub> electrode for NO<sub>3</sub>RR at -0.1 V vs RHE in a flow cell with 1 M KOH + 5 mM KNO<sub>3</sub> electrolyte at a flow rate of 15 mL h<sup>-1</sup>, where *j* represents current density. The error bars represent the standard deviation of three independent measurements.

The CuNW/Co(OH)<sub>2</sub> electrode was then evaluated for continuous NO<sub>3</sub>RR electrolysis at -0.1 V vs RHE using the flow cell. The electrolysis was first performed with 1 M KOH + 5 mM KNO<sub>3</sub> electrolyte at various flow rates. As shown in Figure 5d, the current density on CuNW/Co(OH)<sub>2</sub> increased monotonously from 12.6 to 34.9 mA cm<sup>-2</sup> as the flow rate increased from 15 to 60 mL h<sup>-1</sup>. Meanwhile, NH<sub>3</sub> was the only major product with a negligible NO<sub>2</sub><sup>-</sup> production in the flow rate range, except a small NO<sub>2</sub><sup>-</sup> Faradaic efficiency of 6.3% at 60 mL h<sup>-1</sup>, showing a highly selective NO<sub>3</sub>RR to NH<sub>3</sub> on the CuNW/Co(OH)<sub>2</sub> electrode. Moreover, the slight increase of NO<sub>2</sub><sup>-</sup> selectivity with the flow rate indicates that a fast electrolyte flow can wash away the intermediately produced NO<sub>2</sub><sup>-</sup> and reduce its probability of re-adsorption and reduction on Co sites. This observation further supports the tandem catalytic mechanism proposed above: the transfer of the \*NO<sub>2</sub> intermediates from Cu to Co sites involves NO<sub>2</sub><sup>-</sup> entering the electrolyte. Impressively, the CuNW/Co(OH)<sub>2</sub> electrode achieved a 100% single-pass conversion of NO<sub>3</sub><sup>-</sup> to NH<sub>3</sub> at flow rates from 15 to 45 mL h<sup>-1</sup> and maintained a 92% conversion at a flow rate of 60 mL h<sup>-1</sup> (Figure 5e), demonstrating an ultrahigh efficient conversion of NO<sub>3</sub><sup>-</sup> to NH<sub>3</sub>.

Typical nitrate sources, such as industrial wastewater and polluted ground water, have a NO<sub>3</sub><sup>-</sup> concentration ranging from few to few tens of mM. 49-51 To test the versatility of the developed CuNW/Co(OH)<sub>2</sub> electrode, we further evaluated it for the NO<sub>3</sub>RR in the flow cell with 1 M KOH electrolytes containing various concentrations of NO<sub>3</sub><sup>-</sup> at a fixed flow rate of 15 mL h<sup>-1</sup>. As shown in Figure 5f, the current density on CuNW/Co(OH)<sub>2</sub> exhibited an almost linear increase from 6.3 to 51.2 mA cm<sup>-2</sup> as the NO<sub>3</sub><sup>-</sup> concentration increased from 5 to 50 mM. Meanwhile, an ultrahigh NH<sub>3</sub> Faradaic efficiency with a negligible NO<sub>2</sub><sup>-</sup> production was achieved on the CuNW/Co(OH)<sub>2</sub> electrode in the NO<sub>3</sub><sup>-</sup> concentration range from 5 to 25 mM, despite a slight decrease in the electrolyte with 50 mM NO<sub>3</sub><sup>-</sup>. Encouragingly, the CuNW/Co(OH)<sub>2</sub> electrode achieved a 100% single-pass conversion of NO<sub>3</sub><sup>-</sup> to NH<sub>3</sub> for electrolytes with various NO<sub>3</sub><sup>-</sup> concentrations ranging from 5 to 50 mM (Figure 5g), even with a low concentration of 1 mM (Figure S24) or in a neutral electrolyte (Figure S25), demonstrating a great potential of the electrode for the denitrification of various wastewater sources as well as other versatile applications. As previous studies of NO<sub>3</sub>RR were mainly performed using H-cell, few studies have measured and reported the single-pass conversion rate of NO<sub>3</sub><sup>-</sup> to NH<sub>3</sub>, as shown in Table S1 that summaries the NO<sub>3</sub>RR performance on a variety of recently reported electrocatalysts. Aiming at practical applications of the NO<sub>3</sub>RR electrolysis, we advocate on the development and use of flow cell for the NO<sub>3</sub>RR tests as well as

the report of single-pass conversion rate as a performance metric. Here our work has demonstrated an example on the design of electrocatalyst and flow cell that achieved 100% single-pass conversion of NO<sub>3</sub><sup>-</sup> to NH<sub>3</sub>, which is, to the best of our knowledge, among the most efficient electrocatalytic systems reported to date for single-pass conversion of dilute nitrate sources to ammonia. Moreover, we tested the stability of CuNW/Co(OH)<sub>2</sub> for long-term continuous NO<sub>3</sub>RR electrolysis. As shown in Figure 5h, the CuNW/Co(OH)<sub>2</sub> electrode maintained a nearly complete single-pass conversion of NO<sub>3</sub><sup>-</sup> to NH<sub>3</sub> during a continuous electrolysis of 35 h.

In summary, we demonstrated a rigorous design of Cu- and Co-based tandem electrocatalyst for efficient conversion of dilute nitrate to ammonia. We first screened the most active component for the NO<sub>3</sub><sup>-</sup>-to-NO<sub>2</sub><sup>-</sup> and NO<sub>2</sub><sup>-</sup>-to-NH<sub>3</sub> steps, respectively, and then balanced the activities of two steps by tuning the surface Cu:Co ratio with an optimal tandem architecture. As a result, a tandem catalyst coupling Cu and Co(OH)<sub>2</sub> was developed, which showed much higher activity and NH<sub>3</sub> selectivity than the counterpart catalysts including Cu, Co(OH)<sub>2</sub>, and Cu-Co alloy. Impressively, using a flow cell, the CuNW/Co(OH)<sub>2</sub> electrode achieved a complete single-pass conversion of NO<sub>3</sub><sup>-</sup> to NH<sub>3</sub> at -0.1 V vs RHE, and maintained a nearly 100% conversion for electrolytes with various nitrate concentrations (1–50 mM) and at different flow rates. Such an efficient NO<sub>3</sub>RR electrolysis is facilitated by a tandem mechanism that involves NO<sub>3</sub><sup>-</sup> reduction to NO<sub>2</sub><sup>-</sup> on Cu, indirect transfer of NO<sub>2</sub><sup>-</sup> via the electrolyte, and NO<sub>2</sub><sup>-</sup> reduction to NH<sub>3</sub> on Co-based sites. Our work demonstrates a rigorous design process and principles of tandem electrocatalysts for nitrate reduction and other complex electrochemical reactions, with new mechanistic insights into tandem electrocatalysis.

#### ASSOCIATED CONTENT

## **Supporting Information.**

The Supporting Information is available free of charge at ...

Experimental methods, additional materials characterization and electrochemical measurements (Figures S1–S25, Table S1) (PDF)

#### **AUTHOR INFORMATION**

### **Corresponding Author**

\*E-mail: Xiaofeng.Feng@ucf.edu

**ORCID:** Zhuanghe Ren: 0000-0002-0858-2987

Kaige Shi: 0000-0003-1372-0210

Xiaofeng Feng: 0000-0002-9473-2848

**Notes:** The authors declare no competing financial interest.

#### **ACKNOWLEDGMENTS**

This material is based upon work supported by the National Science Foundation (NSF) under Grant No. 1943732. Z.R. acknowledges the support from the Preeminent Postdoctoral Program (P3) at the University of Central Florida. We acknowledge the use of an XPS instrument supported by the NSF MRI: ECCS: 1726636. Use of the Stanford Synchrotron Radiation Lightsource, SLAC National Accelerator Laboratory, is supported by the U.S. Department of Energy, Office of Science, Office of Basic Energy Sciences under Contract No. DE-AC02-76SF00515. We thank Dr. Parag Banerjee for very helpful discussions.

#### **REFERENCES**

- 1. Canfield, D. E.; Glazer, A. N.; Falkowski, P. G. The evolution and future of Earth's nitrogen cycle. *Science* **2010**, *330*, 192–196.
- 2. Choudhary, M.; Muduli, M.; Ray, S. A comprehensive review on nitrate pollution and its remediation: conventional and recent approaches. *Sustain. Water Resour. Manag.* **2022**, *8*, 113.
- 3. Galloway, J. N.; Townsend, A. R.; Erisman, J. W.; Bekunda, M.; Cai, Z.; Freney, J. R.; Martinelli, L. A.; Seitzinger, S. P.; Sutton, M. A. Transformation of the nitrogen cycle: recent trends, questions, and potential solutions. *Science* **2008**, *320*, 889–892.
- 4. Zeng, Y.; Priest, C.; Wang, G.; Wu, G. Restoring the nitrogen cycle by electrochemical reduction of nitrate: progress and prospects. *Small Methods* **2020**, *4*, 2000672.
- 5. Wang, Y.; Wang, C.; Li, M.; Yu, Y.; Zhang, B. Nitrate electroreduction: mechanism insight, in situ characterization, performance evaluation, and challenges. *Chem. Soc. Rev.* **2021**, *50*, 6720–6733.
- 6. van Langevelde, P. H.; Katsounaros, I.; Koper, M. T. Electrocatalytic nitrate reduction for sustainable ammonia production. *Joule* **2021**, *5*, 290–294.
- 7. Lim, J.; Fernández, C. A.; Lee, S. W.; Hatzell, M. C. Ammonia and nitric acid demands for fertilizer use in 2050. *ACS Energy Lett.* **2021**, *6*, 3676–3685.

- 8. Hu, L.; Pillai, H. S.; Feit, C.; Shi, K.; Gao, Z.; Banerjee, P.; Xin, H.; Feng, X. Identification of active sites for ammonia electrosynthesis on ruthenium. *ACS Energy Lett.* **2022**, *7*, 4290–4298.
- 9. Yang, X.; Mukherjee, S.; O'Carroll, T.; Hou, Y.; Singh, M. R.; Gauthier, J. A.; Wu, G. Achievements, challenges, and perspectives on nitrogen electrochemistry for carbon-neutral energy technologies. *Angew. Chem. Int. Ed.* **2023**, *62*, e202215938.
- 10. He, W.; Zhang, J.; Dieckhöfer, S.; Varhade, S.; Brix, A. C.; Lielpetere, A.; Seisel, S.; Junqueira, J. R. C.; Schuhmann, W. Splicing the active phases of copper/cobalt-based catalysts achieves high-rate tandem electroreduction of nitrate to ammonia. *Nat. Commun.* 2022, 13, 1129.
- 11. Pérez-Gallent, E.; Figueiredo, M. C.; Katsounaros, I.; Koper, M. T. M. Electrocatalytic reduction of nitrate on copper single crystals in acidic and alkaline solutions. *Electrochim. Acta* **2017**, *227*, 77–84.
- 12. Liu, J. X.; Richards, D.; Singh, N.; Goldsmith, B. R. Activity and selectivity trends in electrocatalytic nitrate reduction on transition metals. *ACS Catal.* **2019**, *9*, 7052–7064.
- 13. Chen, G. F.; Yuan, Y.; Jiang, H.; Ren, S. Y.; Ding, L. X.; Ma, L.; Wu, T.; Lu, J.; Wang, H. Electrochemical reduction of nitrate to ammonia via direct eight-electron transfer using a copper–molecular solid catalyst. *Nat. Energy* **2020**, *5*, 605–613.
- 14. Wang, Y.; Zhou, W.; Jia, R.; Yu, Y.; Zhang, B. Unveiling the activity origin of a copper-based electrocatalyst for selective nitrate reduction to ammonia. *Angew. Chem. Int. Ed.* **2020**, *59*, 5350–5354.
- 15. Fu, X.; Zhao, X.; Hu, X.; He, K.; Yu, Y.; Li, T.; Tu, Q.; Qian, X.; Yue, Q.; Wasielewski, M. R.; Kang, Y. Alternative route for electrochemical ammonia synthesis by reduction of nitrate on copper nanosheets. *Appl. Mater. Today* **2020**, *19*, 100620.
- 16. Jia, R.; Wang, Y.; Wang, C.; Ling, Y.; Yu, Y.; Zhang, B. Boosting selective nitrate electroreduction to ammonium by constructing oxygen vacancies in TiO<sub>2</sub>. *ACS Catal.* **2020**, *10*, 3533–3540.
- 17. Hu, T.; Wang, C.; Wang, M.; Li, C. M.; Guo, C. Theoretical insights into superior nitrate reduction to ammonia performance of copper catalysts. *ACS Catal.* **2021**, *11*, 14417–14427.
- 18. Wang, Y.; Qin, X.; Shao, M. First-principles mechanistic study on nitrate reduction reactions on copper surfaces: Effects of crystal facets and pH. *J. Catal.* **2021**, *400*, 62–70.

- 19. Lim, J.; Liu, C. Y.; Park, J.; Liu, Y. H.; Senftle, T. P.; Lee, S. W.; Hatzell, M. C. Structure sensitivity of Pd facets for enhanced electrochemical nitrate reduction to ammonia. *ACS Catal.* **2021**, *11*, 7568–7577.
- Harmon, N. J.; Rooney, C. L.; Tao, Z.; Shang, B.; Raychaudhuri, N.; Choi, C.; Li, H.; Wang, H. Intrinsic catalytic activity of carbon nanotubes for electrochemical nitrate reduction. *ACS Catal.* 2022, 12, 9135–9142.
- 21. Lim, J.; Chen, Y.; Cullen, D. A.; Lee, S. W.; Senftle, T. P.; Hatzell, M. C. PdCu electrocatalysts for selective nitrate and nitrite reduction to nitrogen. *ACS Catal.* **2023**, *13*, 87–98.
- 22. Barrera, L.; Silcox, R.; Giammalvo, K.; Brower, E.; Isip, E.; Bala Chandran, R. Combined effects of concentration, pH, and polycrystalline copper surfaces on electrocatalytic nitrate-to-ammonia activity and selectivity. *ACS Catal.* **2023**, *13*, 4178–4192.
- 23. Ren, Z.; Shi, K.; Feng, X. Elucidating the intrinsic activity and selectivity of Cu for nitrate electroreduction. *ACS Energy Lett.* **2023**, *8*, 3658–3665.
- 24. Mattarozzi, L.; Cattarin, S.; Comisso, N.; Gambirasi, A.; Guerriero, P.; Musiani, M.; Vázquez-Gómez, L.; Verlato, E. Hydrogen evolution assisted electrodeposition of porous Cu-Ni alloy electrodes and their use for nitrate reduction in alkali. *Electrochim. Acta* 2014, 140, 337–344.
- Wang, Y.; Xu, A.; Wang, Z.; Huang, L.; Li, J.; Li, F.; Wicks, J.; Luo, M.; Nam, D. H.; Tan, C. S.; et al. Enhanced nitrate-to-ammonia activity on copper-nickel alloys via tuning of intermediate adsorption. *J. Am. Chem. Soc.* 2020, 142, 5702–5708.
- 26. Yuan, J.; Xing, Z.; Tang, Y.; Liu, C. Tuning the oxidation state of Cu electrodes for selective electrosynthesis of ammonia from nitrate. *ACS Appl. Mater. Interfaces* **2021**, *13*, 52469–52478.
- 27. Chen, F. Y.; Wu, Z. Y.; Gupta, S.; Rivera, D. J.; Lambeets, S. V.; Pecaut, S.; Kim, J. Y. T.; Zhu, P.; Finfrock, Y. Z.; Meira, D. M.; et al. Efficient conversion of low-concentration nitrate sources into ammonia on a Ru-dispersed Cu nanowire electrocatalyst. *Nat. Nanotechnol.* 2022, 17, 759–767.
- 28. Gao, Q.; Pillai, H. S.; Huang, Y.; Liu, S.; Mu, Q.; Han, X.; Yan, Z.; Zhou, H.; He, Q.; Xin, H.; Zhu, H. Breaking adsorption-energy scaling limitations of electrocatalytic nitrate

- reduction on intermetallic CuPd nanocubes by machine-learned insights. *Nat. Commun.* **2022**, *13*, 338.
- 29. Gao, Q.; Yao, B.; Pillai, H. S.; Zang, W.; Han, X.; Liu, Y.; Yu, S. W.; Yan, Z.; Min, B.; Zhang, S.; et al. Synthesis of core/shell nanocrystals with ordered intermetallic single-atom alloy layers for nitrate electroreduction to ammonia. *Nat. Synth.* **2023**, *2*, 624–634.
- 30. Li, P.; Li, R.; Liu, Y.; Xie, M.; Jin, Z.; Yu, G. Pulsed nitrate-to-ammonia electroreduction facilitated by tandem catalysis of nitrite intermediates. *J. Am. Chem. Soc.* **2023**, *145*, 6471–6479.
- 31. Zhou, N.; Wang, Z.; Zhang, N.; Bao, D.; Zhong, H.; Zhang, X. Potential-induced synthesis and structural identification of oxide-derived Cu electrocatalysts for selective nitrate reduction to ammonia. *ACS Catal.* **2023**, *13*, 7529–7537.
- 32. Paliwal, A.; Bandas, C. D.; Thornburg, E. S.; Haasch, R. T.; Gewirth, A. A. Enhanced nitrate reduction activity from Cu-alloy electrodes in an alkaline electrolyte. *ACS Catal.* **2023**, *13*, 6754–6762.
- 33. Fu, Y.; Wang, S.; Wang, Y.; Wei, P.; Shao, J.; Liu, T.; Wang, G.; Bao, X. Enhancing electrochemical nitrate reduction to ammonia over Cu nanosheets via facet tandem catalysis. *Angew. Chem. Int. Ed.* **2023**, *62*, e202303327.
- 34. Liu, C.; Zhang, G.; Zhang, W.; Gu, Z.; Zhu, G. Specifically adsorbed ferrous ions modulate interfacial affinity for high-rate ammonia electrosynthesis from nitrate in neutral media. *Proc. Natl. Acad. Sci. U.S.A.* **2023**, *120*, e2209979120.
- 35. Wang, X.; Wu, X.; Ma, W.; Zhou, X.; Zhang, S.; Huang, D.; Winter, L. R.; Kim, J. H.; Elimelech, M. Free-standing membrane incorporating single-atom catalysts for ultrafast electroreduction of low-concentration nitrate. *Proc. Natl. Acad. Sci. U.S.A.* **2023**, *120*, e2217703120.
- 36. Zhang, J.; He, W.; Quast, T.; Junqueira, J. R. C.; Saddeler, S.; Schulz, S.; Schulmann, W. Single-entity electrochemistry unveils dynamic transformation during tandem catalysis of Cu<sub>2</sub>O and Co<sub>3</sub>O<sub>4</sub> for converting NO<sub>3</sub><sup>-</sup> to NH<sub>3</sub>. *Angew. Chem. Int. Ed.* **2022**, *62*, e202214830.
- 37. Jeon, T. H.; Wu, Z. Y.; Chen, F. Y.; Choi, W.; Alvarez, P. J.; Wang, H. Cobalt–copper nanoparticles on three-dimensional substrate for efficient ammonia synthesis via electrocatalytic nitrate reduction. *J. Phys. Chem. C* **2022**, *126*, 6982–6989.

- 38. Fu, W.; Du, Y.; Jing, J.; Fu, C.; Zhou, M. Highly selective nitrate reduction to ammonia on CoO/Cu foam via constructing interfacial electric field to tune adsorption of reactants. *Appl. Catal. B* **2023**, *324*, 122201.
- 39. Gao, W.; Xie, K.; Xie, J.; Wang, X.; Zhang, H.; Chen, S.; Wang, H.; Li, Z.; Li, C. Alloying of Cu with Ru enabling the relay catalysis for reduction of nitrate to ammonia. *Adv. Mater.* **2023**, *35*, e2202952.
- 40. Han, S.; Li, H.; Li, T.; Chen, F.; Yang, R.; Yu, Y.; Zhang, B. Ultralow overpotential nitrate reduction to ammonia via a three-step relay mechanism. *Nat. Catal.* **2023**, *6*, 402–414.
- 41. Murphy, E.; Liu, Y.; Matanovic, I.; Guo, S.; Tieu, P.; Huang, Y.; Ly, A.; Das, S.; Zenyuk, I.; Pan, X.; et al. Highly durable and selective Fe- and Mo-Based atomically dispersed electrocatalysts for nitrate reduction to ammonia via distinct and synergized NO<sub>2</sub><sup>-</sup> pathways. *ACS Catal.* **2022**, *12*, 6651–6662.
- 42. Shi, N.; Gao, J.; Li, K.; Li, Y.; Zhang, W.; Yang, Q.; Jiang, B. Upcycling wastewater nitrate into ammonia fertilizer via concurrent electrocatalysis and membrane extraction. *Chem. Eng. J.* **2023**, *455*, 140959.
- 43. Xu, Z.; Wan, L.; Liao, Y.; Pang, M.; Xu, Q.; Wang, P.; Wang, B. Continuous ammonia electrosynthesis using physically interlocked bipolar membrane at 1000 mA cm<sup>-2</sup>. *Nat. Commun.* **2023**, *14*, 1619.
- 44. McEnaney, J. M.; Blair, S. J.; Nielander, A. C.; Schwalbe, J. A.; Koshy, D. M.; Cargnello, M.; Jaramillo, T. F. Electrolyte engineering for efficient electrochemical nitrate reduction to ammonia on a titanium electrode. *ACS Sustain. Chem. Eng.* **2020**, *8*, 2672–2681.
- 45. Wu, Z. Y.; Karamad, M.; Yong, X.; Huang, Q.; Cullen, D. A.; Zhu, P.; Xia, C.; Xiao, Q.; Shakouri, M.; Chen, F. Y.; et al. Electrochemical ammonia synthesis via nitrate reduction on Fe single atom catalyst. *Nat. Commun.* **2021**, *12*, 2870.
- 46. Li, P.; Jin, Z.; Fang, Z.; Yu, G. A single-site iron catalyst with preoccupied active centers that achieves selective ammonia electrosynthesis from nitrate. *Energy Environ. Sci.* **2021**, *14*, 3522–3531.
- 47. Fan, K.; Xie, W.; Li, J.; Sun, Y.; Xu, P.; Tang, Y.; Li, Z.; Shao, M. Active hydrogen boosts electrochemical nitrate reduction to ammonia. *Nat. Commun.* **2022**, *13*, 7958.

- 48. Zhang, S.; Wu, J.; Zheng, M.; Jin, X.; Shen, Z.; Li, Z.; Wang, Y.; Wang, Q.; Wang, X.; Wei, H.; Zhang, J. Fe/Cu diatomic catalysts for electrochemical nitrate reduction to ammonia. *Nat. Commun.* **2023**, *14*, 3634.
- 49. Ascott, M. J.; Gooddy, D. C.; Wang, L.; Stuart, M. E.; Lewis, M. A.; Ward, R. S.; Binley, A. M. Global patterns of nitrate storage in the vadose zone. *Nat. Commun.* **2017**, *8*, 1416.
- 50. Nguyen, T. T. P.; Do, B. K. D.; Bui, N. N.; Pham, M. A.; Nguyen, T. B. Selectiveness of copper and polypyrrole modified copper electrodes for nitrate electroreduction: a comparative study and application in ground water. *ECS Trans.* **2013**, *53*, 41–52.
- 51. Chauhan, R.; Srivastava, V. C. Electrochemical denitrification of highly contaminated actual nitrate wastewater by Ti/RuO<sub>2</sub> anode and iron cathode. *Chem. Eng. J.* **2020**, *386*, 122065.
- 52. Kim, K. H.; Lee, H.; Huang, X.; Choi, J. H.; Chen, C.; Kang, J. K.; O'Hare, D. Energy-efficient electrochemical ammonia production from dilute nitrate solution. *Energy Environ. Sci.* **2023**, *16*, 663–672.
- 53. Wang, S.; Petzold, V.; Tripkovic, V.; Kleis, J.; Howalt, J. G.; Skulason, E.; Fernández, E. M.; Hvolbæk, B.; Jones, G.; Toftelund, A.; et al. Universal transition state scaling relations for (de) hydrogenation over transition metals. *Phys. Chem. Chem. Phys.* **2011**, *13*, 20760–20765.
- 54. Zhao, T.; Jiang, H.; Ma, J. Surfactant-assisted electrochemical deposition of α-cobalt hydroxide for supercapacitors. *J. Power Sources* **2011**, *196*, 860–864.
- 55. Yang, J.; Liu, H.; Martens, W. N.; Frost, R. L. Synthesis and characterization of cobalt hydroxide, cobalt oxyhydroxide, and cobalt oxide nanodiscs. *J. Phys. Chem. C* **2010**, *114*, 111–119.
- 56. Liu, Y. C.; Koza, J. A.; Switzer, J. A. Conversion of electrodeposited Co(OH)<sub>2</sub> to CoOOH and Co<sub>3</sub>O<sub>4</sub>, and comparison of their catalytic activity for the oxygen evolution reaction. *Electrochim. Acta* **2014**, *140*, 359–365.
- 57. Larson, P. E. X-ray induced photoelectron and auger spectra of Cu, CuO, Cu<sub>2</sub>O, and Cu<sub>2</sub>S thin films. *J. Electron Spectrosc. Relat. Phenom.* **1974**, *4*, 213–218.
- 58. Choi, H. C.; Jung, Y. M.; Noda, I.; Kim, S. B. A study of the mechanism of the electrochemical reaction of lithium with CoO by two-dimensional soft X-ray absorption spectroscopy (2D XAS), 2D Raman, and 2D heterospectral XAS-Raman correlation analysis. *J. Phys. Chem. B* **2003**, *107*, 5806–5811.

- 59. Searle, P. L. The Berthelot or indophenol reaction and its use in the analytical chemistry of nitrogen. *Analyst* **1984**, *109*, 549–568.
- 60. Green, L. C.; Wagner, D. A.; Glogowski, J.; Skipper, P. L.; Wishnok, J. S.; Tannenbaum, S. R. Analysis of nitrate, nitrite, and [<sup>15</sup>N] nitrate in biological fluids. *Anal. Biochem.* **1982**, *126*, 131–138.
- 61. Wang, H.; Yang, Y.; DiSalvo, F. J.; Abruña, H. D. Multifunctional electrocatalysts: Ru–M (M = Co, Ni, Fe) for alkaline fuel cells and electrolyzers. *ACS Catal.* **2020**, *10*, 4608–4616.
- 62. Kim, H.; Park, H.; Oh, S.; Kim, S. K. Facile electrochemical preparation of nonprecious Co-Cu alloy catalysts for hydrogen production in proton exchange membrane water electrolysis. *Int. J. Energy Res.* **2020**, *44*, 2833–2844.
- 63. Ma, M.; Djanashvili, K.; Smith, W. A. Selective electrochemical reduction of CO<sub>2</sub> to CO on CuO-derived Cu nanowires. *Phys. Chem. Chem. Phys.* **2015**, *17*, 20861–20867.
- 64. Shi, K.; Willis, M. D.; Ren, Z.; Feng, X. Efficient recycling of dilute nitrate to ammonia using Cu nanowire electrocatalyst. *J. Phys. Chem. C* **2023**, *127*, 20710–20717.

# **Table of Contents (TOC) Graphic:**

